Combined effect of heterogeneity, anisotropy and saturation on steady state flow and transport: Structure recognition and numerical simulation

N. Ursino

Dipartimento di Ingegneria Idraulica, Marittima, Ambientale e Geotecnica, University of Padova, Padova, Italy

T. Gimmi

Paul Scherrer Institute (PSI), Villigen, Switzerland

Rock-Water Interaction Group (RWI), Institute of Geological Sciences, University of Bern, Bern, Switzerland

Received 19 March 2003; revised 15 September 2003; accepted 3 October 2003; published 21 January 2004.

[1] Natural soil profiles may be interpreted as an arrangement of parts which are characterized by properties like hydraulic conductivity and water retention function. These parts form a complicated structure. Characterizing the soil structure is fundamental in subsurface hydrology because it has a crucial influence on flow and transport and defines the patterns of many ecological processes. We applied an image analysis method for recognition and classification of visual soil attributes in order to model flow and transport through a man-made soil profile. Modeled and measured saturation-dependent effective parameters were compared. We found that characterizing and describing conductivity patterns in soils with sharp conductivity contrasts is feasible. Differently, solving flow and transport on the basis of these conductivity maps is difficult and, in general, requires special care for representation of small-scale processes. *INDEX TERMS:* 1875 Hydrology: Unsaturated zone; 1866 Hydrology: Soil moisture; 1869 Hydrology: Stochastic processes; 1894 Hydrology: Instruments and techniques; *KEYWORDS:* anisotropy, structures, unsaturated media

Citation: Ursino, N., and T. Gimmi (2004), Combined effect of heterogeneity, anisotropy and saturation on steady state flow and transport: Structure recognition and numerical simulation, *Water Resour. Res.*, *40*, W01514, doi:10.1029/2003WR002180.

1. Introduction

[2] At the catchment and river basin scales the soil moisture patterns influence runoff, soil mechanics, subsurface transport and plants evolution. Because of the dynamics of water in soil and across the atmosphere-soil interface, the hydrological systems may swoop between different states [e.g., *Grayson et al.*, 1997; *Western et al.*, 2001]. The switching from one state to another depends on climate and soil storage and on their interaction [e.g., *Western et al.*, 2002]. To link the spatial structure of the soil moisture field and its fluctuation in time with the climatic forcing and the environmental conditions are some of the main challenges of this decade [*Rodriguez-Iturbe*, 2000; *Fernandez-Illescas et al.*, 2001]. In field soils, preferential flow appears to be the rule rather than the exception [*Jury and Flühler*, 1992]. This statement is supported by many tracer experiments that had been carried out at the field scale to investigate relevant transport processes in soils [e.g., *Butters et al.*, 1989; *Flury et al.*, 1994; *Forrer et al.*, 1999; *Vanderborght et al.*, 2001].

[3] The intermediate scale, between the pore and the field scale, is a suitable playground for observing and modeling processes that take place also at the larger scale. In particular, tank experiments performed in the laboratory under controlled conditions [e.g., *Wildenschild and Jensen*, 1999; *Walter et al.*, 2000] are very valuable. *Ursino et al.* [2001a, 2001b] observed in a tracer experiment in a quasi two dimensional tank, an artificial, heterogeneous soil profile made out of sandy structures (thin layers), swooping from a mildly heterogeneous state under wet conditions, to a state characterized by highly preferential paths under drier conditions.

[4] Emerging new techniques for remote structure detection are expected to be helpful in validating and improving hydrological models at very different scales. A growing effort is going to produce significant advances in the field of tomography for microstructure detection [e.g., *Clausnitzer and Hopmans*, 1999]. At a much larger scale, remotely sensed data provide detailed information on soil morphology and soil moisture patterns [e.g., *Chen et al.*, 2001; *Engman*, 2000]. *Tidwell and Wilson* [2002] quantitatively compared the local permeability of three rock cubes at each point to various statistical measures of the digital rock image at the same point. The spatial statistics of all three rock samples confirmed the similarity of spatial patterns in the permeability maps and digital images, even if establishing a relation between conductivity and visual attributes of the sample was difficult.

[5] We focus here on two major problems related to the tank experiment of *Ursino et al.* [2001a, 2001b]: structure recognition and modeling the different states of soil that depend on the average soil moisture. An image analysis

0043-1397/04/2003WR002180

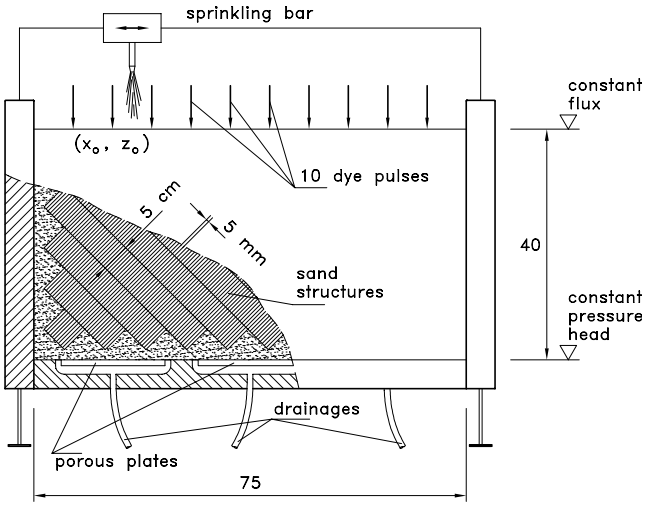

Figure 1. Setup of the tank experiment and relevant scales (the dimensions of the tank are expressed in centimeters).

procedure (T. Gimmi and N. Ursino, Estimating the material distribution in a heterogeneous laboratory sand tank by image analysis, submitted to *Soil Science Society of America Journal*, 2003) (hereinafter referred to as Gimmi and Ursino, submitted manuscript, 2003) was applied to the image of the tank, where many fine layers randomly filled with three different sands constitute the structures of an artificial soil profile. The structures were extracted based on the first two moments of the gray level within a moving window. Every point of the image of the profile was then related to a sand type. The conductivity and retention curves of the three sands were determined by column experiments. Flow and transport within the tank were tackled numerically with a continuum approach and compared with the results of the previous dye tracer experiments.

2. Summary of the Results of the Previous Experiment and Relevant Scales

[6] Transport in a quasi two-dimensional random field with a strong anisotropy of the conductivity correlation structure was observed under different mean saturation degrees [*Ursino et al.*, 2001a]. Figure 1 illustrates the experimental setup. The upper boundary condition was: constant flux $Q = 5.2 \times 10^{-6}$, 3.2×10^{-6} and 1.3×10^{-6} m $\times$ s^{-1}, respectively, for the case of high-flow rate (HFR), intermediate-flow rate (IFR), and low-flow rate (LFR). The lower boundary condition was: constant matric head $\Psi = -0.25$ m. Steady flow only was considered. Ten pulses of a dye were applied evenly distributed over the tank surface. Pictures of the developing plumes were taken at irregular time intervals, and the first two moments of the dye displacement were evaluated by image analysis (see *Ursino et al.* [2001a] for more details). The main results were the following.

[7] 1. Low saturation led to strongly preferential flow: the transport was fast and almost parallel to the bedding, indicating an extremely anisotropic conductivity tensor (evaluated according to *Stephens and Heerman* [1988] for the whole tank). Spreading of dye was very large, especially in the direction parallel to the mean flow [*Ursino et al.*, 2001a].

[8] 2. Mixing, quantified by the dilution index [*Kitanidis*, 1994], was almost unaffected by the average saturation, not evidencing any preferential mixing regime [*Ursino et al.*, 2001b].

[9] At least four relevant scales can be distinguished for the tank experiment: (1) the pore scale (comparable with the sand grain size, ranging from 0.08 to 0.9 mm); (2) the scale of the smaller correlation length of the conductivity identified by the thickness of individual sand layers (0.5 cm); (3) the scale of the larger correlation length of the conductivity, corresponding to the layer length (5 cm); (4) the tank scale (40 $\times$ 75 cm) that represents the field scale.

[10] In the present work, we denote as effective parameters those defined for the whole horizontal cross section of the tank. Average breakthrough curves were calculated to define an effective homogeneous one dimensional convection-dispersion model that has the same first and second travel time moments as the heterogeneous medium. The following effective parameters represent the heterogeneity of the tank as a whole: effective anisotropy of the conductivity tensor, effective volumetric water content, and effective dispersivity (see Section 5). We compared numerical and experimental estimates of the effective parameters to explore whether, on the basis of a very detailed soil structure description, commonly used codes and modeling approaches easily capture the features observed in the tank; in particular, the fast channelized flow and transport leading to high spreading of dye without significant local mixing. Such flow regimes, which establish at certain saturation degrees only, may have significant effects on the environment and its complex dynamics.

3. Image Analysis Applied to Soil Structure Recognition

[11] Back scattering of light and thus the gray levels of the image of a soil surface depend on its properties like texture, surface roughness, and chemical composition. Image analysis coupled with soil sampling and measuring properties of soil samples, may be a valuable tool for characterization of a soil profile. We applied an image analysis procedure as described basically by Gimmi and Ursino (submitted manuscript, 2003) to obtain the two-dimensional distribution of sands in our artificial profile. We only give a brief outline of the procedure here and refer to the above paper for details and a general discussion.

[12] First, the inhomogeneity of the illumination and reflection had to be corrected. This was done by using two images successively as flat fields: an image of a gray cardboard in front of the tank, and an image of the tank, corrected according to the first flat field and smoothed with a mean filter with a large window, such that all structural features were eliminated. The segmentation and classification of the image was based on soil color and soil texture, which were estimated as mean and variance or coefficient of variation of the gray levels within a filter window. Soil texture was in our case defined by the grain sizes, because our original image resolution (pixel size of about 0.7 mm $\times$ 0.7 mm) was of the same order as the grain sizes of the three sands (0.08–0.2 mm, 0.1–0.5 mm, and 0.3–0.9 mm). For each pixel of the corrected image, a vector of characteristic features was obtained that contained the mean, the variance, the mode and the coefficient of variation of the gray levels

Table 1. Reference Vectors Used for Automatic Sand Recognition by Image Analysis[a]

	Mean Mode	Variance	MeanSquared Mean Error	Mean Squared Variance Error	CV
VFS	63	5	0.03	0.85	0.03
FS	71	22	0.05	0.07	0.07
CS	56	35	0.06	0.05	0.09

[a]VFS, FS, and CS indicate very fine, fine, and coarse sands, respectively.

within the filter window. In order to preserve the typical shape of sand layers, we used a diagonal, layer shaped filter window with 9 elements.

[13] Reference vectors for the three sands were obtained by sampling the image at 50 locations for each sand, where the type of sand was known. The reference vectors obtained in this way are listed in Table 1. Mean and mode were identical for each sand. The classification consisted of finding the reference vector with the minimum distance to each pixel vector. The classification was only accepted when the distance was below a threshold value of half the distance between the two reference vectors closest to each other. Because the very fine sand had clearly the lowest variance, double weight was attributed to the variance and coefficient of variation in a first classification scan to separate the very fine from the other sands. In a second scan, the mean was weighted double to assign the remaining pixels to the fine or the coarse sand.

[14] The soil map at the end of these classification scans was not complete, because a number of pixels were not within the threshold distance to one of the reference vectors. We filled the remaining gaps by a modal, layer shaped filter. Morphological closing operations could be performed to homogenize additionally the layer shaped areas attributed to one of the sands, as described by Gimmi and Ursino (submitted manuscript, 2003). For the simulations, the resolution of the sand map was reduced from the original size by a factor of three by a modal filter. The corrected image of the sand tank and the soil map obtained after classification are shown in Figures 2 and 3, respectively.

4. Multistep Column Experiments to Estimate Hydraulic Parameters of Sands

[15] A series of multistep out- and inflow experiments [e.g., *Eching and Hopmans*, 1993] was performed to estimate the hydraulic properties of the three sands. Plexiglas columns with an inner diameter of 5.4 cm and a filter plate at the bottom were carefully filled with sand to a height of about 34 cm using the same filling tube as for preparing the layers of the heterogeneous tank. The columns were equipped with three Time Domain Reflectometry (TDR) waveguides (7.5, 17.5, and 30.2 cm above the filter plate) and three tensiometers (5.0, 13.5, and 19.0 cm above the filter plate). The TDR sensors were connected to a CASMI-TDR (Easy Test, Lublin, Poland) device, which allowed automatic recording of the travel times t_s of an electromagnetic wave through the sand. From t_s the dielectric number ϵ_c was calculated as

$$\epsilon_c = \left(\frac{t_s - t_0}{t_{ref} - t_0}\right)^2 \epsilon_{ref}, \quad (1)$$

where t_0 was the previously determined offset of the TDR signal, t_{ref} the travel time in water serving as a reference medium, and ϵ_{ref} the dielectric number of water. Volumetric water contents θ were then estimated from ϵ_c with the relation of *Topp and Davies* [1985],

$$\theta = -0.053 + 0.0292\epsilon_c - 5.5 \times 10^{-4}\epsilon_c^2 + 4.3 \times 10^{-6}\epsilon_c^3. \quad (2)$$

The tensiometers were connected to pressure transducers that allowed also an automatic recording.

[16] The columns were saturated for several days before the water table was lowered in 5 to 10 steps to 40 to 67 cm below the filter plate, and consequently raised again in 4 to 5 steps to the top of the sand filling. A desaturation-saturation cycle lasted, depending on the sand, between about 2 to 12 days. The top of the column was protected against evaporation during that time.

[17] The measured transient responses in matric head and water content were analyzed with the code HYDRUS 5.0 [*Vogel et al.*, 1996], which was coupled to a Levenberg-Marquardt algorithm [*Press et al.*, 1992] to optimize the hydraulic parameters. The hydraulic properties of the sands were described with the model of *Vogel and Cislerova* [1988], which is a slight modification of the Mualem-van Genuchten model (see manual of HYDRUS 5.0 for details;

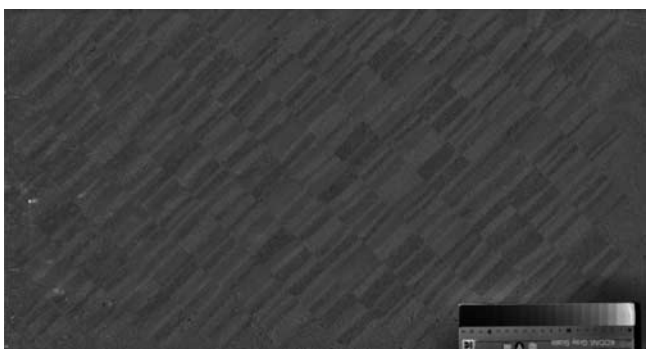

Figure 2. Sand structures. Image corrected for inhomogeneous illumination and used to derive the soil map by image analysis.

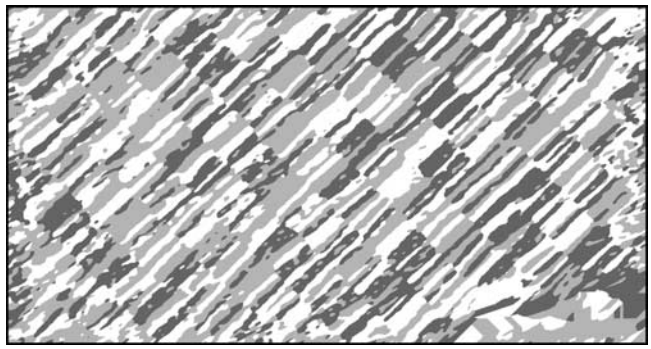

Figure 3. Sand structures. Recognition by image analysis. Light shading corresponds to fine sand (FS), medium shading corresponds to very fine sand (VFS), and dark shading corresponds to coarse sand (CS).

Table 2. Hydraulic Parameters for the Three Sands: Very Fine Sand (VFS), Fine Sand (FS), and Coarse Sand (CS)[a]

	K_{sw}, cm/d	K_{sd}, cm/d	θ_r	θ_s	θ_m	n	α_w, 1/cm	α_d, 1/cm
CS								
Value	4500	4800	2.0e-2	3.20e-1	3.21e-1	12.0	1.1e-1	6.3e-2
Standard error							1.7e-4	6.8e-5
FS								
Value	1100	1300	2.0e-2	3.30e-1	3.31e-1	9.2	7.6e-2	3.6e-2
Standard error						5.2e-2	1.0e-4	5.2e-5
VFS								
Value	260	380	0.0	3.50e-1	3.51e-1	6.6	4.7e-2	2.0e-2
Standard error						3.0e-3	5.0e-6	9.6e-6

[a]If a standard error is given, the parameter was optimized based on a multistep experiment. Note that the reported standard errors are very likely too low since some systematic deviations between measured and fitted curves for some sensors were found that could not be eliminated with the used water flow model.

the additional parameter θ_a included by *Vogel and Cislerova* [1988] was set to θ_r):

$$\theta = \theta_r + \frac{\theta_m - \theta_r}{[1 + |\alpha h|^n]^m} \quad (\text{for } h < h_s)$$
$$\theta = \theta_s \quad (\text{for } h \geq h_s) \tag{3}$$

and

$$K(h) = K_s \left(\frac{\theta - \theta_r}{\theta_s - \theta_r}\right)^{0.5} \left[\frac{1 - F(\theta)}{1 - F(\theta_s)}\right]^2 (\text{for } h < h_s)$$
$$K(h) = K_s \quad (\text{for } h \geq h_s) \tag{4}$$

where $n > 1$ can be regarded as a pore size distribution index, $m = 1 - 1/n$, θ_s is the water content at saturation, θ_m an extrapolated parameter slightly larger than θ_s, h_s the (nonzero) capillary height at θ_s, and

$$F(\theta) = \left[1 - \left(\frac{\theta - \theta_r}{\theta_m - \theta_r}\right)^{1/m}\right]^m. \tag{5}$$

When $\theta_m = \theta_s$, the above model reduces to the original Mualem-van Genuchten form. A θ_m slightly larger than θ_s generally improves numerical stability, but has nearly no effect on the hydraulic functions for large values of n. Hysteresis was accounted for by assuming different values of α and K_s, namely α_d and α_w, and K_{sd} and K_{sw}, for drying and wetting, respectively (see manual of HYDRUS 5.0 for details).

[18] Only the parameters α_d, α_w, and n were estimated from the measured data. The water content and matric head measurements were inversely weighted by their respective uncertainties and by their number, such that each data set had in the end the same relative weight. The water content at saturation, θ_s, was fixed to the largest observed water content for each sand, θ_m to a slightly larger value, and the residual water content θ_r to zero or 0.02 (see Table 2). For the coarse sand, the parameter n tended to relatively large values (>10). In this range, serious numerical problems may occur due to the appearance of a sharp kink near saturation in the hydraulic conductivity function. Because the overall shape of the conductivity function in the dryer region is only slightly affected by further increases of n, we fixed n finally at a value of 12 for the coarse sand to circumvent the numerical problems. The saturated hydraulic conductivities were obtained from a series of independent experiments, where the water flux through the column at a given gradient was measured. For the evaluation of K_s the known flow resistance of the filter plate at the bottom was taken into account. For each sand, the largest measured value was assigned to K_{sd}, the smallest to K_{sw}.

[19] The hydraulic parameters obtained in this way are listed in Table 2. Overall, the correspondence between measured and simulated temporal responses was acceptable, even though some systematic discrepancies for certain sensors occurred. The fitting turned out to be quite difficult because of numerical problems encountered in case of large n values. The reported standard errors for the fitted parameters are based on standard deviations of 1 cm for the matric heads and 0.01 for the water contents. Figure 4 shows the estimated water retention curves together with measured data. Because no data pairs water content/matric head were obtained at exactly the same depths, the matric heads at 19.0

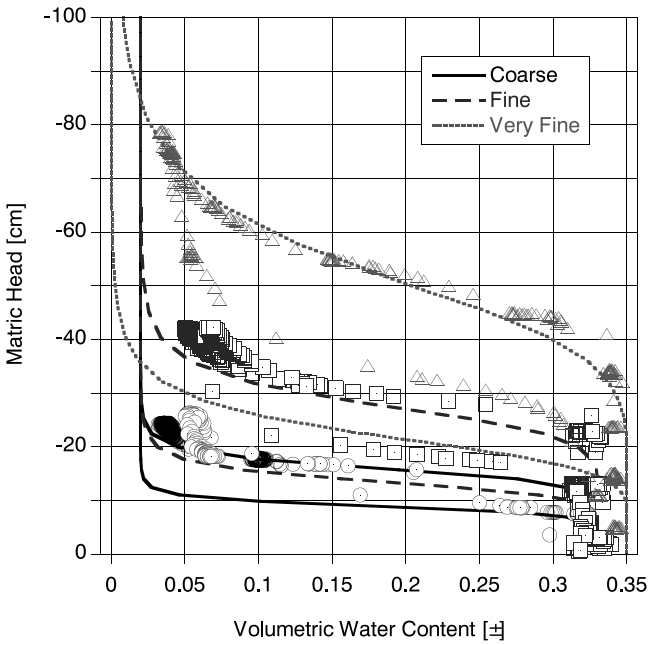

Figure 4. Estimated water retention functions for the three sands and measurements. Triangles are used for very fine sand, squares are for fine sand, and circles are for coarse sand. Note that the shown measured matric head and water contents were not obtained exactly at the same locations and therefore may slightly differ from the estimated functions.

and 5.0 cm above the filter plate were corrected by −1.5 and +2.5 cm, respectively, and plotted versus the water contents at 17.5 and 7.5 cm. This allows a rough comparison although, of course, no exact match between these partly adjusted data and the estimated functions can be expected. One has to keep two things in mind, when looking at the differences between measurements and calculated curves. First, the lines show the fitted main drying and main wetting curves (the hysteretic envelope), whereas the symbols represent data from the main drying branch and from a scanning wetting curve. The latter naturally falls somewhere in between the two main curves. Second, not all data that were used in the fitting procedure can be shown in Figure 4. The discrepancies between the displayed data and the fitted curves are partly forced by data values at other measurement locations.

5. Numerical Simulation of Flow and Transport

[20] The steady state flow of water in unsaturated media is governed by the steady state form of the Richards equation:

$$\nabla \cdot [K(h)\nabla(h - z)] = 0, \tag{6}$$

where the vertical coordinate z is positive downward. The hydraulic conductivity $K(h)$ is defined here at a scale smaller than a single sand layer and is therefore isotropic. The heterogeneous sand distribution is shown in Figure 3, and the sand properties are indicated in Table 2.

[21] The mass balance equation for the solute is:

$$\frac{\partial[\theta C]}{\partial t} + \nabla \cdot [\theta \mathbf{V} C] - \nabla \cdot [\theta \mathbf{D} \nabla C] = 0, \tag{7}$$

where C is the solute concentration in the pore water, and $\mathbf{V} = (V_x, V_z) = -K(h)\ \nabla\ (h - z)/\theta$ is the pore velocity. The local dispersion tensor $\mathbf{D}$ is given by a constant D_0 accounting for isotropic molecular diffusion and by a term proportional to the absolute value of the pore velocity [*Bear*, 1972]:

$$D_{ij} = [\alpha_l - \alpha_t]\frac{V_i V_j}{|\mathbf{V}|} + [\alpha_t |\mathbf{V}| + D_0]\delta_{ij}. \tag{8}$$

[22] The effect of the local dispersivities α_l and α_t is generally minor as compared to hydrodynamic dispersion in heterogeneous media. Commonly, for the size of our sand tank and the sands with grain sizes lower than about 0.1 cm, the longitudinal local dispersivity α_l is set in the range of 0 to 1 cm, whereas the transverse dispersivity α_t may be about one order of magnitude lower. We did not have enough elements to estimate the local dispersivity from the experiment. On the basis of previous results [*Ursino et al.*, 2001b] we believe that local dispersivity is about the same at the LFR, when water flows almost exclusively through the fine sand, and at the HFR, when water flows across the structures through the three different sands. Also, the grain sizes of the sands were not very different and thus we decided to consider two cases: very low ($\alpha_l = \alpha_t = 0.001$ cm) and low isotropic local dispersivity ($\alpha_l = \alpha_t = 0.05$ cm). Molecular diffusion was neglected in the simulations.

[23] The three steady flow conditions (HFR, IFR, and LFR) observed in the laboratory experiment that was described in section 2, were simulated with the finite element code SWMS [*Simunek et al.*, 1994]. Then, the transport problem was solved by particle tracking [*Roth and Hammel*, 1996]. Particles were injected over all the soil surface, starting at a reasonable distance from the boundary. Effective parameters (the effective anisotropy of the conductivity tensor, the effective volumetric water content, and effective dispersivities), which represent the heterogeneity of the medium as a whole, were calculated as described in the next paragraph and were conveniently used to compare the simulated and experimental results.

[24] The first and second travel time moments at the tank scale for an effective one-dimensional convection-dispersion model were inferred from calculated breakthrough curves. They were obtained for a concentration $C(t)$ at the upper boundary described by a Dirac pulse, solving numerically the mass balance equation (7) for the solute. On the basis of the average arrival time and displacement, the anisotropy ratio A (the conductivity parallel divided by the conductivity perpendicular to the layering) and the mean vertical component V_z of the pore velocity are defined as [*Ursino et al.*, 2001a]:

$$A = \frac{\tan\beta}{\tan\gamma} \tag{9}$$

and

$$V_z = \frac{d\langle z\rangle}{dt}. \tag{10}$$

where $\langle z\rangle$ is the average vertical displacement of the tracer particles and $\langle x\rangle$, the average horizontal displacement; $\alpha = atan\left(\frac{d\langle x\rangle}{d\langle z\rangle}\right)$ is the direction of the mean trajectory; $\gamma = 45°$ is the angle between the bedding and the horizontal direction, and $\beta = \alpha + \gamma$ is the angle between the mean trajectory and the direction perpendicular to the bedding. The specific discharge, V_z/Q, is the ratio between the mean vertical centroid velocity and the upper boundary discharge. It is the inverse of the volumetric water content that participates in flow.

[25] The effective vertical dispersivity defines the spread of solute travel distances around the average travel depth $\langle z\rangle$, at a certain time [*Jury and Sposito*, 1985]:

$$\alpha_z^{eff} = \frac{var[z - \langle z\rangle]}{2\langle z\rangle}, \tag{11}$$

or, alternatively, the spread of solute travel time around the average solute travel time $\langle t\rangle$ at a certain depth [*Roth and Hammel*, 1996]:

$$\alpha_z^{eff} = \frac{\langle z\rangle var[t - \langle t\rangle]}{2\langle t\rangle^2}, \tag{12}$$

where $t(z)$ is the time when the generic particle reaches the depth z, and $var[.]$ denotes the variance of the property in brackets.

[26] Similarly, the effective horizontal dispersivity defines the spread of solute travel distances around the

average horizontal travel distance [*Roth and Hammel*, 1996].

$$\alpha_x^{eff} = \frac{var[x - \langle x \rangle]}{2\langle z \rangle} \tag{13}$$

where $[x - \langle x \rangle]$ is the horizontal displacement of the generic particle at time t from the average horizontal particle position, and $var[x - \langle x \rangle]$ is its variance.

6. Results and Discussion

[27] There were two main problems connected with the numerical simulation of flow through the heterogeneous profile considered here: (1) to find the right compromise between an accurate description of the soil map (Figure 3) and a necessarily limited CPU time; (2) the computational problems when simulating the very dry condition, which were caused by the very steep hydraulic conductivity functions.

[28] The first problem can be tackled by reducing the resolution of the very detailed soil map. Reducing it to a size larger than the structure elements is a very complex problem of attributing equivalent larger scale parameters to coarse grids. We kept the grid scale smaller than the smaller correlation length of the structures, and thus did not face any upscaling problem. In order to limit the computational effort (in terms of CPU time), the image resolution was reduced from 204 pixels/cm^2 (Figure 3) to 22.6 pixels/cm^2 (reduction by a factor of three in both dimensions), leading to a grid spacing of 0.21 cm (the thickness of the finest layers was 0.5 cm).

[29] Simulating flow through sands with such Mualem-van Genuchten parameters as those obtained from the multistep outflow experiment was a challenge. In fact, the conductivity may switch within a narrow pressure range from values close to zero to values that are close to the saturated conductivity, and this caused relevant numerical problems. In order to achieve the convergence of the simulation for the LFR we were forced to approach the long term solution (steady state) setting n in the Mualem-van Genuchten equations equal to values lower than the measured ones. Progressively increasing n toward the real values, we derived a series of steady state solutions to be used as an initial condition for the following simulation with larger n. We report here about the cases with $n = (2, 2, 2)$, $n = (2, 3, 4)$, $n = (2, 5, 6)$, and $n = (2, 6, 8)$, where the first value in parentheses refers to the very fine sand (VFS), the second to the fine sand (FS), and the third to the coarse sand (CS). It was not possible to achieve convergence adopting the estimated n values indicated in Table 2. The relative unsaturated conductivity K/K_s as a function of the matric head h is plotted in Figure 5 for $n = (2, 2, 2)$, $n = (2, 6, 8)$ and for the real $n = (6.6, 9.2, 12.0)$. The discrepancies of the conductivity functions for the FS and the CS when $n = 6$ and 8 instead of 9.2 and 12 were small and thus were expected to have minor effect on flow and transport. For the VFS, the discrepancies when $n = 2$ instead of 6.6 are larger, but are expected to be of minor effect also, because the layers of this sand were always at a relatively high saturation.

6.1. Anisotropy and Vertical Specific Discharge (First-Order Moments of the Displacement)

[30] The anisotropy and the mean vertical velocity (equations (9) and (10)) estimated numerically for the LFR using

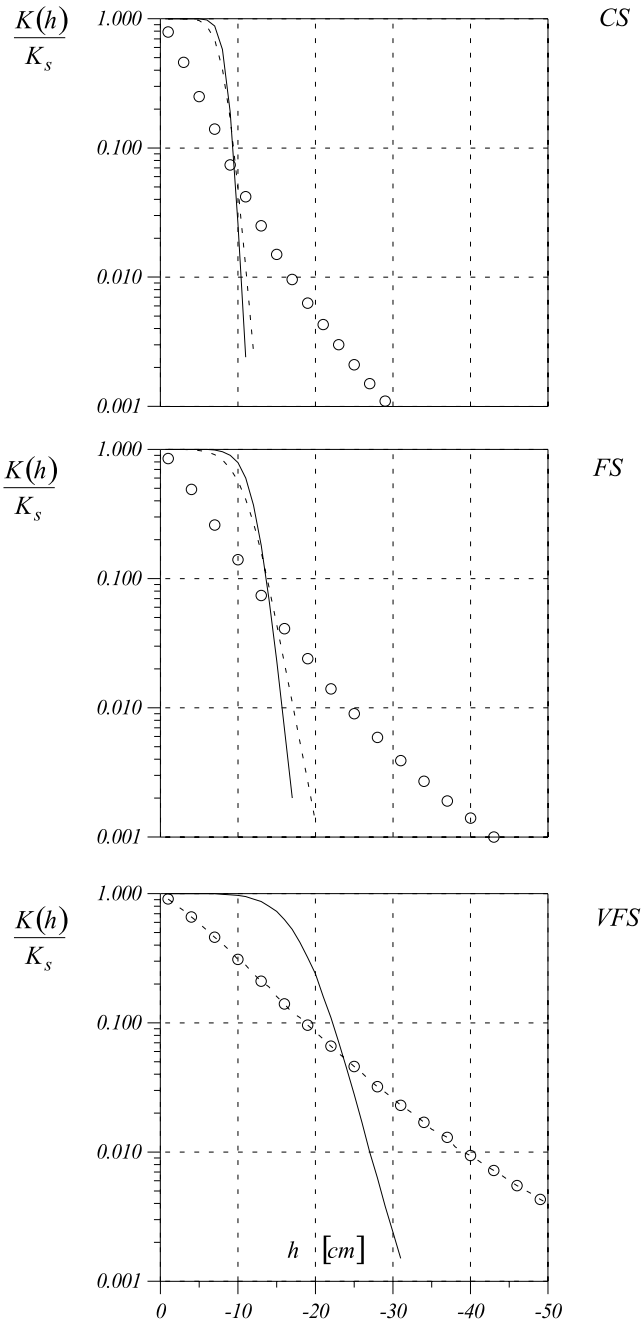

Figure 5. Relative unsaturated conductivity as a function of matric head. Estimated $n = (6.6, 9.2, 12.0)$ (solid line), cases of $n = (2, 2, 2)$ (circles), and $n = (2, 6, 8)$ (dashed line). Top to bottom: coarse sand (CS), fine sand (FS), and very fine sand (VFS).

different n are shown in Figure 6. The corresponding anisotropy and specific discharge evaluated by image analysis for the tank experiment were respectively 570 and 13.6 [*Ursino et al.*, 2001a]. While, by increasing n, we approached higher (but not high enough) anisotropy factors we apparently always overestimated the specific discharge and underestimated anisotropy.

[31] In the following we further analyze the case with $n = (2, 6, 8)$, that was considered as an upper limit for n within the range of parameters that ensured the convergence of the

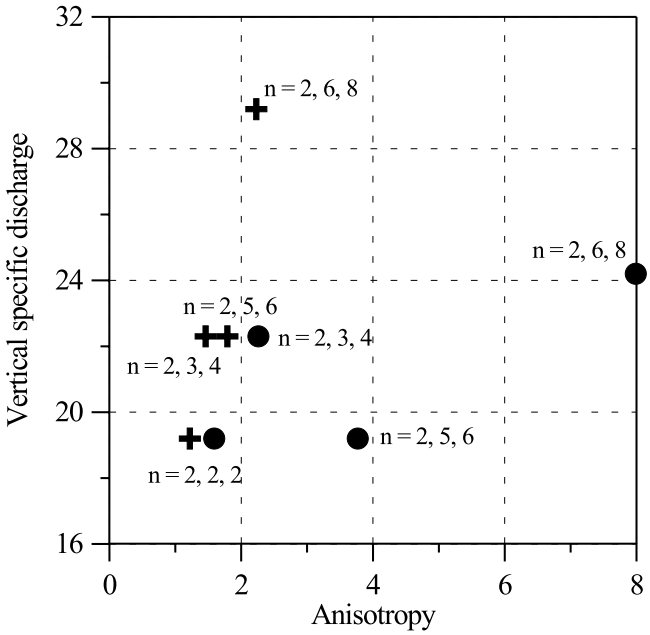

Figure 6. Vertical specific discharge and anisotropy evaluated in case of LFR for different soil parameters. Cases of $\alpha_l = \alpha_t = 0.001$ cm (crosses) and $\alpha_l = \alpha_t = 0.05$ cm (circles). The labels indicate the values attributed to n in the Mualem-van Genuchten equation to very fine, fine, and coarse sand, respectively. The experimental values for the anisotropy and for the specific discharge, evaluated by image analysis, were 570 and 13.6, respectively [*Ursino et al.*, 2001a].

numerical code. The calculated water saturation fields for the three flow rates are shown in Figure 7. Persistent almost saturated paths were always visible. They appeared embedded in a relatively dry matrix in case of the LFR, or coexisted with less saturated parallel flow paths in the other cases.

[32] From now on, results of simulations obtained with negligible local dispersivity ($\alpha_l = \alpha_t = 0.001$ cm) are indicated with solid symbols, results of simulations obtained with small local dispersivity ($\alpha_l = \alpha_t = 0.05$ cm) are indicated with open symbols, and experimental data with open symbols connected by lines (Figures 8, 9, 10, and 11). Circles refer to high-flow rate conditions (HFR), triangles to intermediate-flow rate (IFR) and squares to low+flow rate (LFR).

[33] In Figure 8 the measured and experimentally observed mean depth of the injected particles are represented as a function of time. The slope of the interpolating line represents the vertical component of the mean pore velocity (equation (10)). There are significant differences between measured and simulated mean vertical velocity in the HFR and IFR regimes. The slight increase of the local dispersivity tends to decrease the mean velocity but the improvement is negligible for all flow rates. Finally, the simulated LFR transport is not faster than the IFR, opposite to the experimental evidence. This result suggests that the basic processes that govern the interplay of heterogeneity, hysteresis, and strongly non linear flow and led to fast funneling flow in the tank experiment, are probably missed.

[34] Figure 9 shows the measured and simulated mean trajectories. The mean trajectories of particles (Figure 9) were far from being vertical in both experimental and numerical results. Anisotropy may be estimated based on the mean trajectory according to equation (9). For the LFR regime that was expected to lead to funneled flow, we observed that despite the major difficulties of predicting anisotropy (Figure 6), the correspondence in terms of trajectories seems to be acceptable. Indeed, when the trajectory approaches an angle of 45° to the vertical direction, A becomes very sensitive to even modest variations of the direction of the trajectory. Figure 9 further demonstrates that the small scale dispersion (even if extremely low) has a great influence on the first moment of the horizontal particle displacement, improving the mean trajectory estimate in case of LFR and IFR, but worsening it in case of HFR.

6.2. Comparison of Measured and Evaluated Dispersivity

[35] The available experimental data-set includes first and second moments of the horizontal and vertical dye displacement of ten small plumes injected at different locations on the surface of the tank [*Ursino et al.*, 2001a]. The displace-

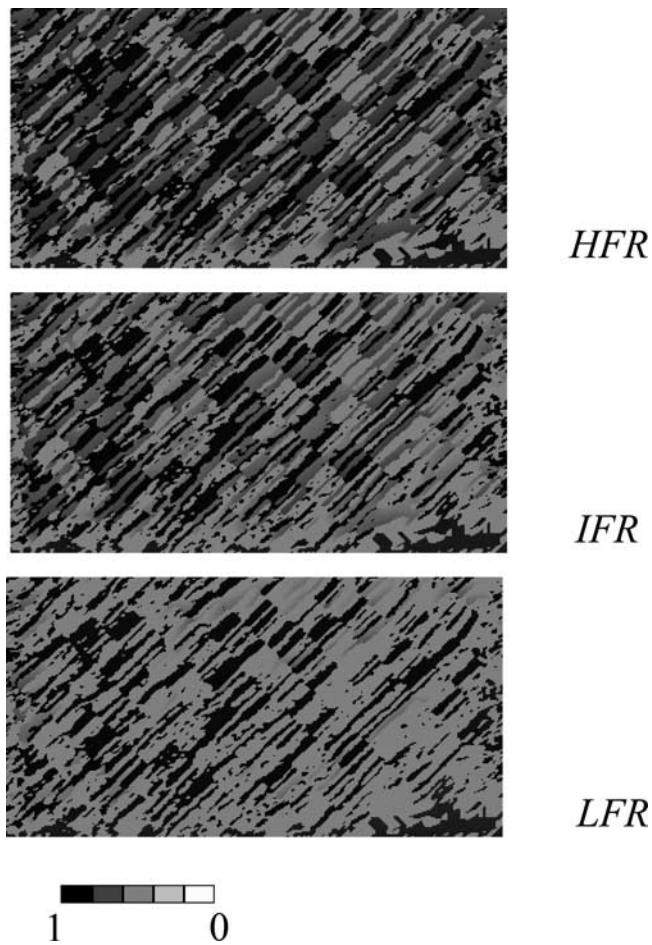

Figure 7. Saturation evaluated by numerical simulation. Light shading corresponds to lower saturation degrees. Top to bottom: high-flow rate (HFR), intermediate-flow rate (IFR), and low-flow rate (LFR).

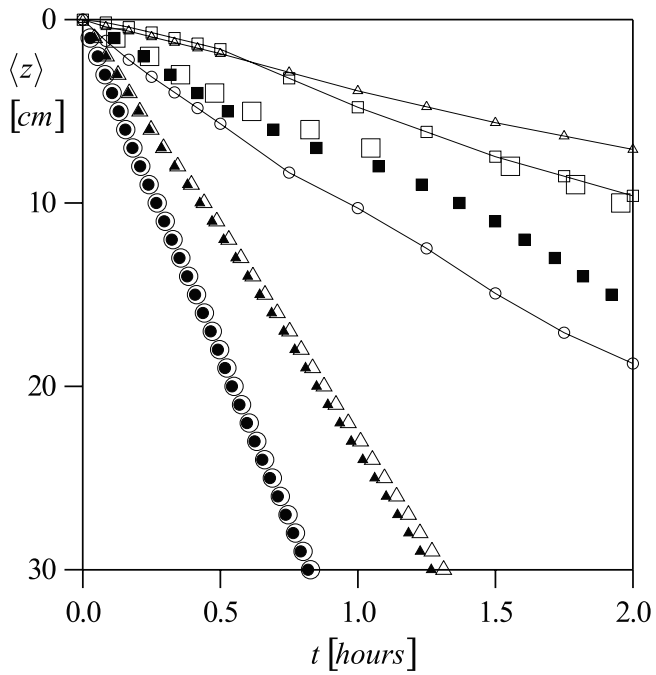

Figure 8. Mean depth versus time, comparison between measured and simulated results. Circles refer to high-flow rate conditions (HFR), triangles refer to intermediate (IFR), and squares refer to low flow rate (LFR). Case of negligible local isotropic dispersivity ($\alpha_l = \alpha_t = 0.001$ cm) is given as solid symbols. Case of very low local isotropic dispersivity ($\alpha_l = \alpha_t = 0.05$ cm) is given as open symbols. Experimental results are given as symbols connected by lines.

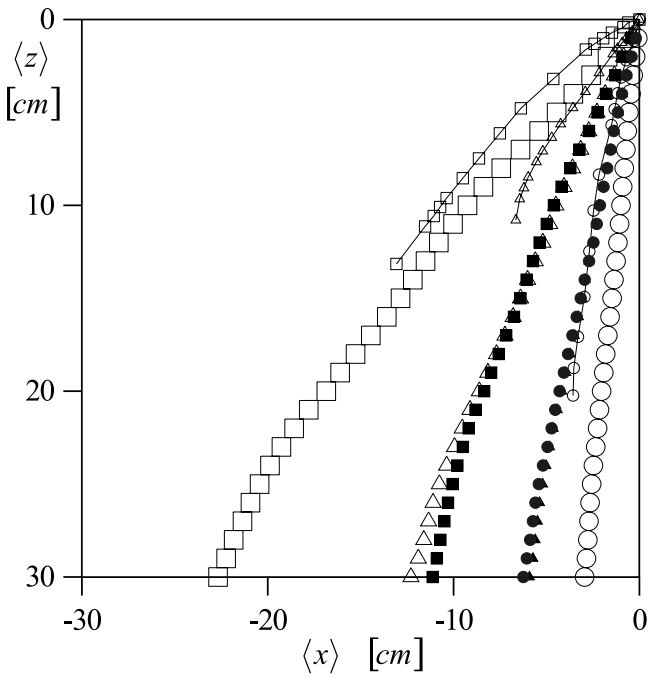

Figure 9. Comparison between measured and simulated mean trajectory. Circles refer to high-flow rate conditions (HFR), triangles refer to intermediate-flow rate (IFR), and squares refer to low-flow rate (LFR). Case of negligible local isotropic dispersivity ($\alpha_l = \alpha_t = 0.001$ cm) is given as solid symbols. Case of very low local isotropic dispersivity ($\alpha_l = \alpha_t = 0.05$ cm) is given as open symbols. Experimental results are given as symbols connected by lines.

ment of a dye particle from the point of injection may be expressed as the sum of three terms: the dye particle displacement from the centroid of a given plume, the displacement of the centroid of the given plume from the mean centroid position of all plumes, i.e., from the average dye particle position, and the displacement of the mean centroid position from the point of injection.

[36] The experimental vertical effective dispersivity indicates the vertical spreading around the average dye particle position and was evaluated as

$$\alpha_z^{eff} = \frac{var\left[z - z_c^i\right] + var\left[z_c^i - \langle z\rangle\right]}{2\langle z\rangle} \tag{14}$$

where $var[z - z_c^i] = \frac{1}{10}\sum_{i=1}^{10} \frac{\int \left(z - z_c^i\right)^2 C^i dxdz}{\int C^i dxdz}$ is the averaged second moment of the vertical displacement around the centroid depth $z_c^i = \frac{\int zC^i dxdz}{\int zC^i dxdz}$ of a single plume i; $var[z_c^i - \langle z\rangle] = \frac{1}{10}\sum_{i=1}^{10}(z_c^i - \langle z\rangle)^2$ is the variance of the vertical displacement of the 10 centroids around the mean vertical displacement, and $\langle z\rangle = \frac{1}{10}\sum_{i=1}^{10} z_c^i$ is the average dye particle position. No cross terms appear in (14) since the 10 plumes were considered as statistically representative and thus $\int (z - z_c^i)\ \langle z\rangle\ C^i dxdz = \int (z - z_c^i)\ z_c^i C^i dxdz = 0$ and $\frac{1}{10}\sum_{i=1}^{10}(z_c^i - \langle z\rangle\ \langle z\rangle) = 0$.

[37] Similarly, the experimental horizontal effective dispersivity, which represents the horizontal spreading around

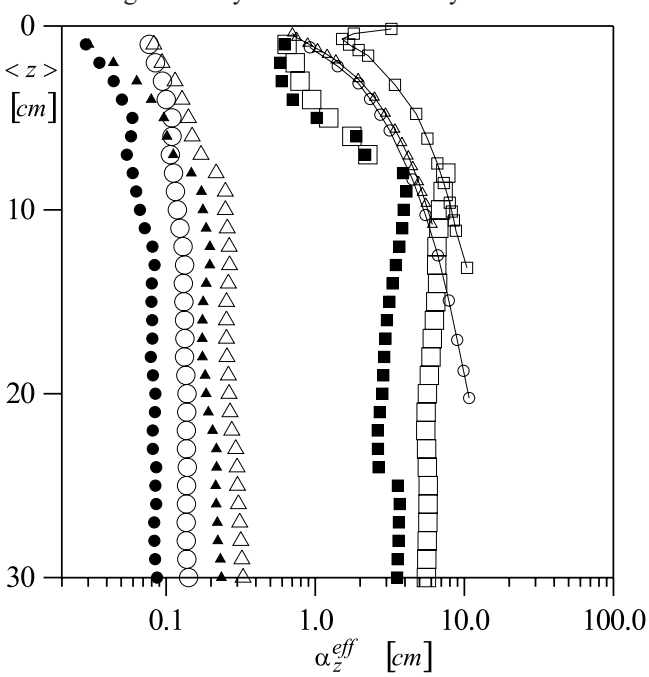

Figure 10. Comparison between measured and simulated effective vertical dispersivity. Circles refer to high-flow rate conditions (HFR), triangles refer to intermediate-flow rate (IFR), and squares refer to low-flow rate (LFR). Case of negligible local isotropic dispersivity ($\alpha_l = \alpha_t = 0.001$ cm) is given as solid symbols. Case of very low local isotropic dispersivity ($\alpha_l = \alpha_t = 0.05$ cm) is given as open symbols. Experimental results are given as symbols connected by lines.

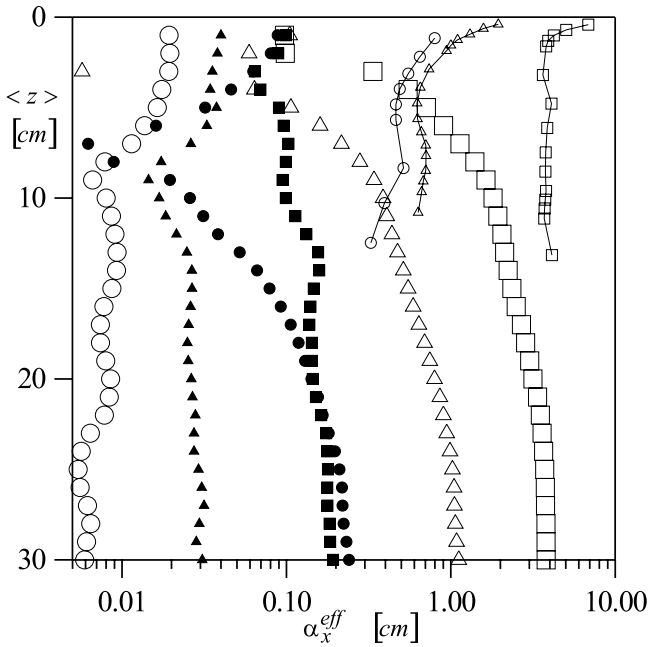

Figure 11. Comparison between measured and simulated effective horizontal dispersivity. Circles refer to high-flow rate conditions (HFR), triangles refer to intermediate-flow rate (IFR), and squares refer to low-flow rate (LFR). Case of negligible local isotropic dispersivity ($\alpha_l = \alpha_t = 0.001$ cm) is given as solid symbols. Case of very low local isotropic dispersivity ($\alpha_l = \alpha_t = 0.05$ cm) is given as open symbols. Experimental results are given by symbols connected by lines.

the average horizontal dye particle position, was evaluated as

$$\alpha_x^{eff} = \frac{var\left[x - x_c^i\right] + var\left[x_c^i - \langle x \rangle\right]}{2\langle z \rangle}, \qquad (15)$$

where $var[x - x_c^i]$ is the averaged second moment of the horizontal displacement around the centroid of a single plume and $var[x_c^i - \langle x \rangle]$ is the variance of the horizontal displacement of the centroids of the 10 plumes around the mean horizontal displacement $\langle x \rangle$ from the point of injection.

[38] Effective vertical and horizontal dispersivities were estimated numerically by particle tracking (equations (12) and (13)) and compared with those of the real plumes [*Ursino et al.*, 2001a] that were evaluated by image analysis according to equations (14) and (15). Vertical and horizontal effective dispersivities are represented respectively in Figures 10 and 11. Major discrepancies between measured and evaluated α_z^{eff} were evidenced in case of IFR and HFR (Figure 10). The agreement between measured and simulated α_x^{eff} was poor in all cases (Figure 11).

[39] Increasing the local dispersivities $\alpha_l = \alpha_t$ improved the estimate of the effective vertical dispersivity in all cases and of the horizontal dispersivity in case of LFR and IFR, but worsened the latter in case of HFR. The same trend was observed for the mean trajectory: The increased subscale dispersivity straightened the trajectories in case of the HFR and caused an underestimation of the horizontal displacement. Apparently, in some cases the prediction of the second-order moments could be improved by fine tuning the local dispersivity. As stated, based on the evaluation of the dilution index [*Ursino et al.*, 2001b] summarized in the Introduction, we expected the local dispersivity to assume comparable values under the three observed transport regimes (LFR, IFR and HFR).

6.3. Comparison of Plume Shapes

[40] On the basis of the calculated effective dispersivities presented in the previous subsection, it appears that adjusting the local dispersivity could be the key for approaching the experimental results in the simulations, even though one has to keep in mind that the soil parameters had to be adjusted to ensure the convergence of the numerical simulation. On the basis of the experimental evaluation of the dilution index [*Ursino et al.*, 2001b], we did not expect the local dispersivity to play such a crucial role in discriminating the physical processes acting at different flow rates.

[41] To further exploit this argument, we compared the images of a plume (instantaneous point-like injection in the center of the upper boundary of the tank, one hour after the injection) in the experimental setup and in the numerical simulation, for the three flow rates (Figures 12 and 13, respectively).

[42] As already shown in Figure 9, the real and simulated plumes reached different depths after a given time from injection. In addition, Figures 12 and 13 show that even though the effective parameters did improve when increasing the small scale dispersivity, the shapes of the simulated plumes differed consistently from the observed ones, being much more smeared in all cases examined.

7. Conclusions

[43] A method to distinguish soil structures by image analysis was applied to a laboratory sand tank. The resulting patchwork of small rectangular elements of three different sands, whose hydraulic properties were separately evaluated by multistep experiments, was used to simulate numerically flow and transport. We encountered major difficulties when trying to simulate flow through the highly heterogeneous structure with the estimated parameters. Numerical problems linked to sharp spatial variation of the conductivity and dry initial conditions are frequently encountered. In the case here we bypassed them by softening the shape of the conductivity function (lowering n) in order to obtain the convergence of the finite element code. This was an arbitrary choice that must be considered with caution, but it may at least give an approximate result.

[44] Our modeling exercise demonstrated that: although the modified soil properties were similar to the measured ones, and the description of the heterogeneous soil structure was accurate, the major large scale effective transport parameters could not be predicted. Among them were the arrival times, the trajectories, and the spreading (Figures 8 to 11). Characterizing the local small scale dispersivity was particularly delicate. In fact, the local dispersivity could be used improperly as a fitting param-

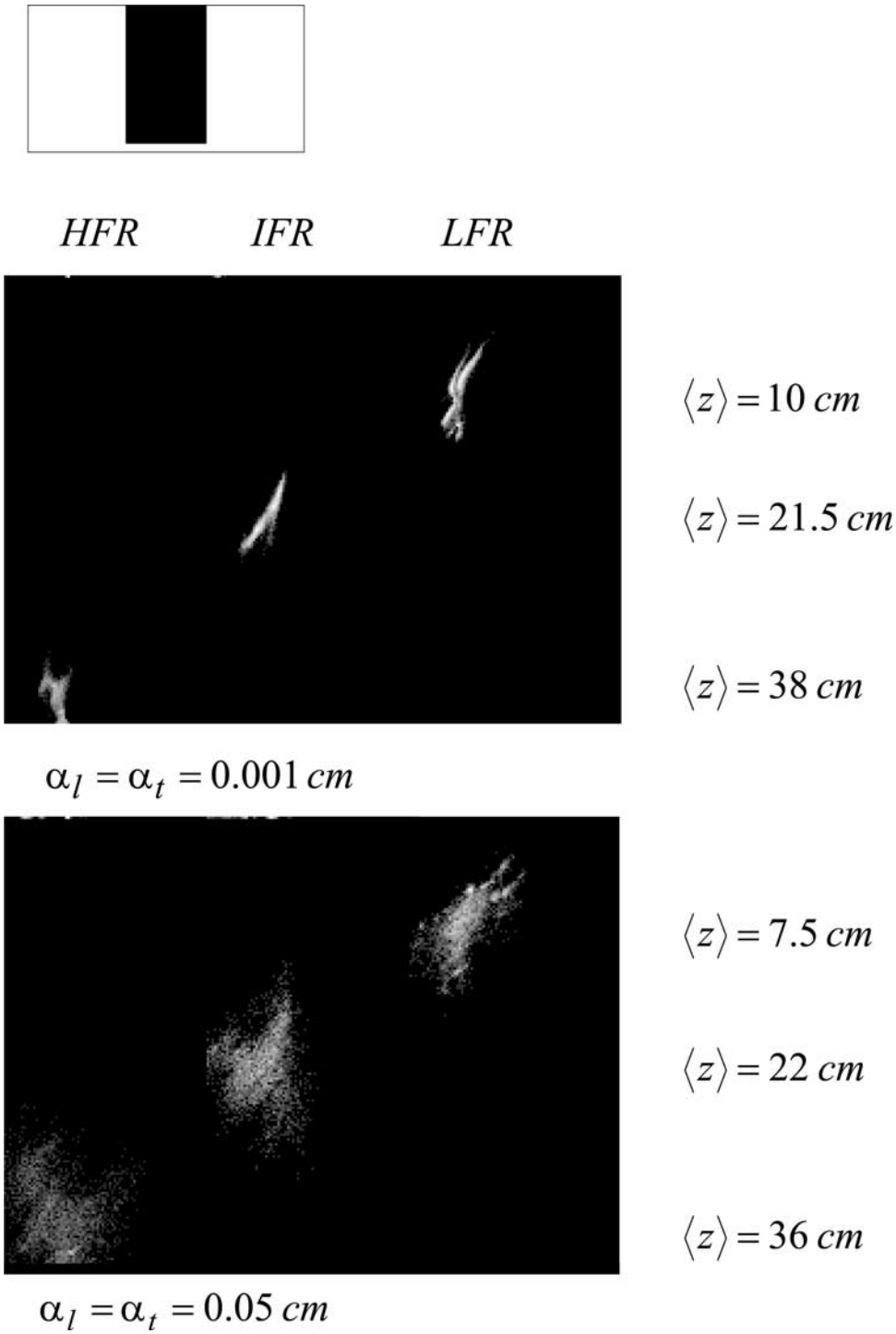

Figure 12. Simulated plumes 1 hour after injection. Mean depth of the centroid $\langle z \rangle$ is indicated for the three cases of HFR, IFR and LFR. (top) $\alpha_l = \alpha_t = 0.001$ cm; (bottom) $\alpha_l = \alpha_t = 0.05$ cm. The images represent the black section of the whole tank as indicated on top.

eter to push the numerical results, in terms of effective parameters, toward the experimental results, but a comparison of the shapes of the plumes (Figures 12 and 13) clearly indicates that this interpretation is not correct.

[45] In summary: We could not obtain the solution of the transport problem using the soil characteristic functions that were determined by the multistep experiments, and used therefore slightly modified functions (Figure 5). The numerical results differed substantially from the experimental evidence. Further advances in numerical modeling may facilitate more accurate studies using the measured parameters, but the discrepancies point, in our opinion, to a more fundamental problem. The continuum approach to model flow and transport through a hetero-

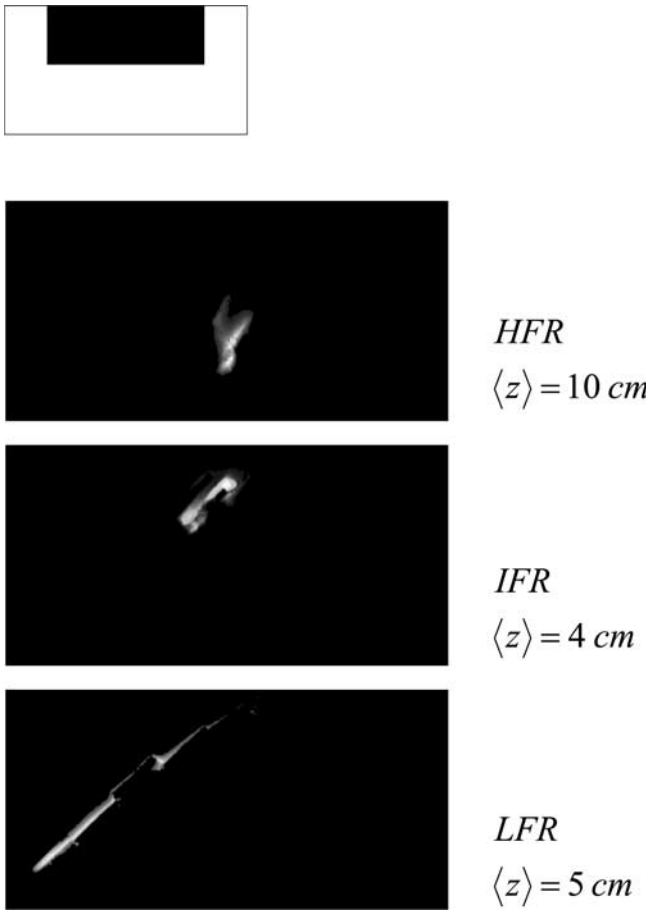

Figure 13. Pictures of the plumes taken during the tank experiment [*Ursino et al.*, 2001a, 2001b] 1 hour after injection. Mean depth of the centroid $\langle z \rangle$ is indicated for the three cases of HFR, IFR, and LFR. The images represent the black section of the whole tank as indicated on top.

geneous medium relies on a certain size of the elements, for which parameters are defined. Going to smaller and smaller scales, or incorporating very fine, possibly important structures in the high-resolution map of the material distribution, may conflict with the requirements of the continuum approach. We cannot exclude that some relevant small scale processes with nonnegligible large scale effects were missed here. For modeling, we chose a scale smaller than the characteristic length of the finer structures, but did not take into account the possible sorting and alignment of materials at the boundaries between layers, and neither entrapped air effects. We did not consider that a thin horizontal redistribution layer could have formed at the top by the impact of the water drops. All these features may have influenced the observed large scale behavior, but it may be difficult to account for them in the frame of a continuum approach. Even if this discussion is limited to a particular study case, we believe that similar problems may affect other cases where flow and transport through structured media is studied at high resolution.

[46] **Acknowledgments.** The numerical work presented here was partially founded by the Jülich Research Centre, Jülich, Germany. Experiments were performed at the Soil Physic Department of the ETH Zürich, Switzerland.

References

Bear, J. (1972), *Dynamics of Fluids in Porous Media*, Elsevier Sci., New York.

Butters, W. L., W. A. Jury, and F. F. Ernst (1989), Field scale transport of bromide in an unsaturated soil. 1 Experimental methodology and results, *Adv. Water Res.*, *25*, 1575–1581.

Chen, J. S., S. Hubbard, and Y. Rubin (2001), Estimating the hydraulic conductivity at the South Oyster Site from geophysical tomographic data using Bayesian techniques based on the normal linear regression model, *Water Resour. Res.*, *37*(6), 1603–1613.

Clausnitzer, V., and J. W. Hopmans (1999), Determination of phase-volume fractions from tomographic measurements in two-phase systems, *Adv. Water Res.*, *22*(6), 577–584.

Eching, S. O., and J. W. Hopmans (1993), Optimization of hydraulic functions from transient outflow and soil water pressure data, *Soil Sci. Soc. Am. J.*, *57*, 1167–1175.

Engmann, E. T. (2000), Soil moisture, in *Remote Sensing in Hydrology and Water Management*, edited by G. A. Schultz and E. T. Engman, pp. 197–216, Spriger-Verlag, New York.

Fernandez-Illescas, C. P., A. Porporato, F. Laio, and I. Rodriguez-Iturbe (2001), The ecohydrological role of soil texture in a water-limited ecosystem, *Water Resour. Res.*, *37*, 2863–2872.

Flury, M., H. Flühler, W. A. Jury, and J. Leuenberger (1994), Susceptibility of soils to preferential flow of water: A field study, *Water Resour. Res.*, *30*, 1945–1954.

Forrer, I., R. Kasteel, M. Flury, and H. Fluhler (1999), Longitudinal and lateral dispersion in unsaturated field soil, *Water Resour. Res.*, *35*, 3049–3060.

Grayson, R. B., A. W. Western, F. H. S. Chiew, and G. Bloschl (1997), Preferred states in spatial soil moisture patterns: Local and nonlocal controls, *Water Resour. Res.*, *33*, 2897–2908.

Jury, W. A., and H. Flühler (1992), Transport of chemicals through soil: Mechanism, models and field application, *Adv. Agron.*, *47*, 141–201.

Jury, W. A., and G. Sposito (1985), Field calibration and validation of solute transport models or the unsaturated zone, *Soil Sci. Soc. Am. J.*, *49*, 1331–1341.

Kitanidis, P. K. (1994), The concept of the dilution index, *Water Resour. Res.*, *30*, 2011–2026.

Press, W. H., P. B. Flannery, S. A. Teukosky, and W. T. Vetterling (1992), *Numerical Recipes in Fortran*, Cambridge Univ. Press, New York.

Rodriguez-Iturbe, I. (2000), Ecohydrology: A hydrologic perspective of climate-soil-vegetation dynamics, *Water Resour. Res.*, *36*, 3–9.

Roth, K., and K. Hammel (1996), Transport of conservative chemical through an unsaturated two-dimensional Miller-similar medium with steady state flow, *Water Resour. Res.*, *32*(6), 1653–1663.

Simunek, J., T. Vogel, and M. T. van Genuchten (1994), The SWMS 2D code for simulating water flow and solute transport in two dimensional variably saturated media, *Res. Rep. 132*, U.S. Salinity Lab., Riverside, Calif.

Stephens, D. B., and S. Heermann (1988), Dependence of anisotropy on saturation in a stratified sand, *Water Resour. Res.*, *24*, 770–778.

Tidwell, V. C., and J. L. Wilson (2002), Visual attributes of a rock and their relationship to permeability: A comparison of digital image and minipermeameter data, *Water Resour. Res.*, *38*(11), 1261, doi:10.1029/2001WR000932.

Topp, G. C., and J. L. Davies (1985), Measurement of soil-water content using time-domain reflectometry (TDR)—A field evaluation, *Soil Sci. Soc. Am. J.*, *49*, 19–24.

Ursino, N., T. Gimmi, and H. Flühler (2001a), Estimating the effect of heterogeneity, anisotropy and saturation on steady state flow and transport in a laboratory sand tank experiment, *Water Resour. Res.*, *37*, 201–208.

Ursino, N., T. Gimmi, and H. Flühler (2001b), Dilution of non-reactive tracers in variably saturated sandy structures, *Adv. Water Res.*, *24*(8), 877–885.

Vanderborght, J., et al. (2001), Overview of inert tracer experiments in a key Belgian soil types: Relation between transport and soil morphological and hydraulic properties, *Water Resour. Res.*, *37*, 2873–2888.

Vogel, T., and M. Cislerova (1988), On the reliability of unsaturated hydraulic conductivity calculated from the moisture retention curve, *Transp. Porous Media*, *3*, 1–15.

Vogel, T., K. Huang, R. Zhang, and M. T. van Genuchten (1996), The HYDRUS code for simulating one-dimensional water flow, solute transport, and heat movement in variably-saturated media, version 5.0, *Res. Rep. 140*, U.S. Salinity Lab., Riverside, Calif.

Walter, M. T., J.-S. Kim, T. S. Steenhuis, J.-Y. Parlange, A. Heilig, R. D. Braddock, J. S. Selker, and J. Boll (2000), Funneled flow mechanisms in a sloping layered soil: Laboratory investigation, *Water Resour. Res.*, *36*, 841–849.

Western, A. W., G. Bloschl, and R. B. Grayson (2001), Toward capturing Hydrologically significant connectivity in spatial patterns, *Water Resour. Res.*, *37*, 83–97.

Western, A. W., R. B. Grayson, and G. Bloschl (2002), Scaling of soil moisture: A hydrologic perspective, *Annu. Rev. Earth Planet. Sci.*, *30*, 149–180.

Wildenschild, D., and K. H. Jensen (1999), Laboratory investigations of effective flow behavior in unsaturated heterogeneous sands, *Water Resour. Res.*, *35*, 17–27.

N. Ursino, Dipartimento di Ingegneria Idraulica, Marittima, Ambientale e Geotecnica, University of Padova, via Loredan 20, 35131 Padova, Italy. (nadia@idra.unipd.it)

T. Gimmi, Paul Scherrer Institute (PSI), CH-5232 Villigen, Switzerland. (thomas.gimmi@psi.ch)